MATERIALS SCIENCE

Molecular orbital imprint in laser-driven electron recollision

Felix Schell,*[†] Timm Bredtmann,*[†] Claus Peter Schulz, Serguei Patchkovskii, Marc J. J. Vrakking, Jochen Mikosch[†]

Electrons released by strong-field ionization from atoms and molecules or in solids can be accelerated in the oscillating laser field and driven back to their ion core. The ensuing interaction, phase-locked to the optical cycle, initiates the central processes underlying attosecond science. A common assumption assigns a single, well-defined return direction to the recolliding electron. We study laser-induced electron rescattering associated with two different ionization continua in the same, spatially aligned, polyatomic molecule. We show by experiment and theory that the electron return probability is molecular frame–dependent and carries structural information on the ionized orbital. The returning wave packet structure has to be accounted for in analyzing strong-field spectroscopy experiments that critically depend on the interaction of the laser-driven continuum electron, such as laser-induced electron diffraction.

INTRODUCTION

The essence of attosecond strong-field spectroscopies and attosecond pulse generation is captured by the well-known and widely used three-step model (1, 2). The three steps consist of laser-driven tunnel ionization, propagation of the electron in the continuum, and interaction with the ion core upon recollision, all of which occur consecutively within a fraction of a laser cycle. While the first two steps are common to all recollision processes, the interaction step can take the form of radiative recombination in high harmonic generation (HHG) or of inelastic or elastic scattering, as is the case in nonsequential double ionization (3–6) and laser-induced electron diffraction (LIED) (7–15). While many experimental observations to date were attributed to the molecular-frame angle dependence of the strong-field ionization (SFI) and the electron-ion interaction steps, one of the central assumptions underlying attosecond strong-field spectroscopies is that the propagation step is largely system-independent. The propagation is usually assumed to "wash out" the phase structure of the initial state, so that the returning wave packet has a well-defined direction of return [for an exception, see the studies of Lein (16) and Meckel et al. (17)]. This assumption is implicitly enforced by the most commonly used quantum-mechanical implementation of the three-step model—the stationary-phase realization of the strong-field approximation (SFA) (18, 19). It is also often assumed that recollision occurs for the same fraction of ionization events, regardless of the molecular orientation [see, however, the study of Morishita and Tolstikhin (20)]. Here, we examine this central proposition both experimentally and theoretically.

We use laser-driven electron rescattering (9) associated with two different SFI continuum channels (21, 22) in the same, spatially laser-aligned 1,3-butadiene molecules. The two channels correspond to different states of the cation formed by SFI and are separated by means of a coincidence measurement. We determine the channel-resolved yields of electrons in the rescattering tail of the photoelectron kinetic energy spectrum in the partially reconstructed molecular frame. We extract their dependence on the alignment of the laser field

relative to the molecule, exploring the polar angle θ, while averaging over the molecular azimuthal angle φ. Both angles are defined in the molecular coordinate system as illustrated in Fig. 1. Access to molecular-frame information is experimentally enabled by deconvolution of laboratory-frame observables that are measured for aligned molecules with the independently determined distribution of molecular alignment. The molecular-frame rescattering yield is given by the product of the molecular-frame ionization probability $S(\theta)$ (23, 24) and the rescattering probability $RQ(\theta)$, which is almost generally assumed to factorize into the return probability $R(\theta)$ and the high-angle scattering probability $Q(\theta)$, following the three-step model. Moreover, in the analysis of strong-field spectroscopy experiments, a common approach is to regard $R(\theta)$ as a constant that does not, hence, depend on θ. $Q(\theta)$ then contains the structural information on the molecule. It captures the molecular-frame dependence of the rescattering differential cross section (DCS), which is extracted in LIED experiments (11, 13, 15, 25). Our approach contains a number of features that are ideally suited for exploration of the returning continuum electron wave packet: (i) The molecular-frame SFI probability $S(\theta)$ is separately determined for the two channels by measuring the yield of direct electrons in the same experiment (24). (ii) The continuum electron wave packets originate from states associated with a different, characteristic nodal structure. (iii) In the interaction step, the channel-dependent returning electron wave packet scatters off the total electron density of the respective cation. Because the electronic structure of the cation differs by the contribution of only one valence electron, $Q(\theta)$ is expected to be nearly the same for the two channels. We explicitly confirm this expectation by a numerical calculation (see below). (iv) The alignment distribution of the sample is the same for the two channels, as these occur in the same molecule.

The SFI of 1,3-butadiene molecules under the conditions used in this study is dominated by two channels accessing the electronic ground (D_0, 90% yield) and the first electronically excited (D_1, 10% yield) state of the 1,3-butadiene cation, as previously established for similar experimental parameters (22, 24). These channels are tagged by formation of the parent ion $C_4H_6^+$ (D_0) and the fragment ions $C_3H_3^+/C_4H_5^+$ (D_1), respectively, with the latter resulting from unimolecular dissociation of the excited cation. The D_0 and D_1 continua correspond to ionization from the HOMO (highest occupied molecular orbital) and HOMO-1. Different SFI continua are understood to

Max-Born-Institut für nichtlineare Optik und Kurzzeitspektroskopie, Max-Born-Strasse 2A, 12489 Berlin, Germany.
*These authors contributed equally to this work.
†Corresponding author. Email: jochen.mikosch@mbi-berlin.de (J.M.); timm.bredtmann@mbi-berlin.de (T.B.)
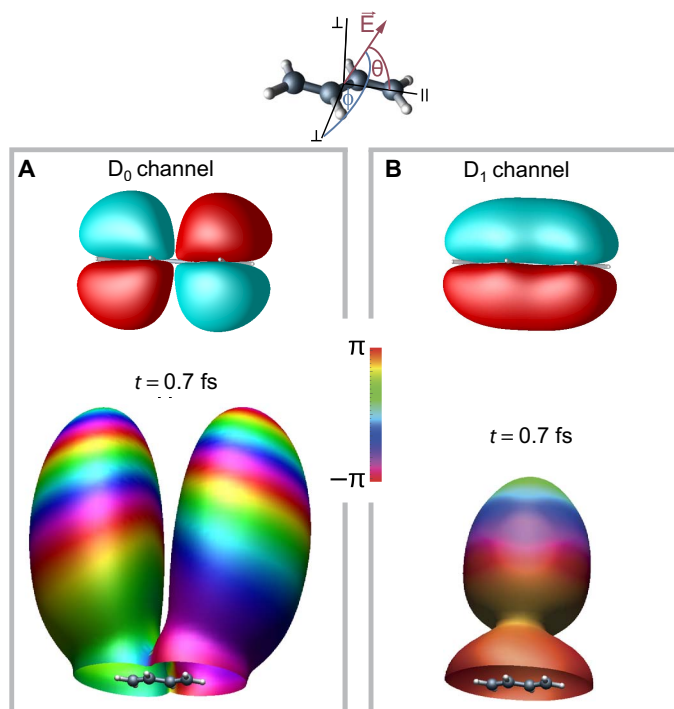
Fig. 1. Channel-specific continuum wave packets in 1,3-butadiene. (A) The upper part shows the D_0 Dyson orbital. The lower part displays a snapshot of the simulated electron density isosurface of value $1.6 \times 10^{-9} a_0^{-3}$ (where a_0 is the Bohr radius) for the D_0 channel 0.7 fs after the peak electric field and was obtained for perpendicular laser polarization ($\theta = 90°$, $\phi = 90°$). The polar angle θ is defined with respect to the principal axis with the lowest moment of inertia, and ϕ is the azimuthal angle (see the coordinate system on top). The color visualizes the phase of the continuum wave function. **(B)** The same as (A) but for the D_1 channel.

be associated with Dyson orbitals $\sqrt{N}\langle\psi_I|\psi_N\rangle$, where ψ_N and ψ_I are the N and $N - 1$ electron wave function of the neutral and the ion, respectively. The Dyson orbitals are hence one-electron wave functions, which are depleted in the SFI step. For the D_0 and D_1 SFI of 1,3-butadiene, the associated Dyson orbitals are depicted in Fig. 1 (A and B). While highly relevant for the structure of the continuum wave packet, the channel-dependent Dyson orbitals contribute only one hole to the overall otherwise-identical electron density distribution of the two states of the 1,3-butadiene molecular ion, which contains a total of 29 electrons. Figure 1 (A and B) also displays the continuum wave packets accompanying D_0 and D_1 SFI. These wave packets are strongly channel-dependent. We will show in the following how the initial nodal structure, which stems from the associated Dyson orbitals, is preserved during propagation.

RESULTS

For the presented experiment, we extended the channel-resolved above-threshold ionization technique (22) to laser-induced rescattering. We used a reaction microscope (26), adjusted to a high photoelectron kinetic energy detection cutoff, to measure the three-dimensional momenta of electrons originating from the SFI of 1,3-butadiene molecules in coincidence with the ion mass. To drive SFI and recollision, linearly polarized laser pulses ($\lambda = 1290$ nm wavelength, 40 fs pulse duration) were used. From the recorded tuples of electron momentum and ion

mass, photoelectron kinetic energy spectra coincident with the formation of $C_4H_6^+$ (D_0), $C_3H_3^+$ (D_1), and $C_4H_5^+$ (D_1) were derived, such as shown in Fig. 2A for a measurement with randomly aligned molecules. The depicted spectra are normalized to the same area. Although the measured yield decreases exponentially with increasing kinetic energy, all distributions contain two regions with different, well-distinguishable slopes for ranges of approximately 0 to 10 eV and above 20 eV. This is the expected behavior separating direct electrons from the rescattering tail. The position of the inflection point located at 16 eV is interpreted as the 2 U_P cutoff for direct electrons and allows us to derive the used intensity, which was $I = (5.2 \pm 1.3) \times 10^{13}$ W/cm^2 for the angle-dependent data (see below). The determined intensity is in good quantitative agreement with the intensity calculated from the laser parameters (see Materials and Methods and the Supplementary Materials). The coincidence spectra in Fig. 2A differ significantly in the relative contribution of the rescattering tail. The rescattering yield is much larger for the electrons coincident with the ions tagging the D_1 as opposed to the ions tagging the D_0 SFI channel. Reassuringly, the measured distributions are the same for the two signature fragments marking D_1, whose yield was combined in the analysis that follows to improve statistics.

To obtain molecular-frame information, we used nonadiabatic laser alignment (27) for one-dimensional field-free spatial alignment of the supersonically cooled molecules. 1,3-Butadiene molecules can be reasonably well described by a symmetric top approximation. Our experiment averages over the azimuthal molecular-frame angle ϕ. A revival trace indicating the measured parent ion yield as a function of Δt, the time delay of the SFI probe pulse with respect to the preceding copolarized alignment laser pulse, is depicted in Fig. 2B. The yield maximizes at $\Delta t = 58$ ps, in line with the expectation for the rotational half-revival. To quantify the degree of alignment, we used a previously established self-consistent procedure in which measured experimental data act as a maximum likelihood predictor for numerical alignment simulations (28). The most probable axis distribution of the aligned molecules is determined together with a confidence interval, which allows the determination of molecular frame–dependent parameters from a deconvolution of laboratory-frame observables that are measured for the aligned molecules. At the delay leading to the maximum SFI yield ($\Delta t = 58$ ps), the peak alignment is reached, characterized by $\langle\cos^2(\theta)\rangle = 0.70^{+0.04}_{-0.07}$ (see the Supplementary Materials for further details). Measurements of the coincidence photoelectron spectrum as a function of α', the angle between the linear polarizations of the alignment and SFI pulses, were performed at peak alignment. α' is labeled with a prime to distinguish this laboratory-frame angle from the unprimed molecular-frame angles.

Using the described procedure, the laboratory-frame angle-dependent yield of direct [$M_D(\alpha')$, 0 to 16 eV] and rescattered [$M_R(\alpha')$, 25 to 55 eV] photoelectrons was determined for the D_0 and D_1 channels, respectively, and is presented in Fig. 2C. Error bars reflect the statistical confidence limits. Molecular-frame (that is, θ-dependent) parameters were determined from the laboratory-frame (that is, α'-dependent) observables by fitting the latter with a series of low-order Legendre polynomials (see solid lines) incorporating the previously determined alignment distribution. The fit of $M_R(\alpha')$ results in the determination of $S(\theta) \times R(\theta) \times Q(\theta)$, the product of the molecular-frame polar angle–dependent ionization, return, and high-angle scattering probabilities. $S(\theta)$ is obtained directly from the deconvolution of $M_D(\alpha')$, the yield of direct electrons. The extracted $S(\theta)$ distributions (see Fig. 3A) resemble the ones reported previously (24), where small quantitative differences are
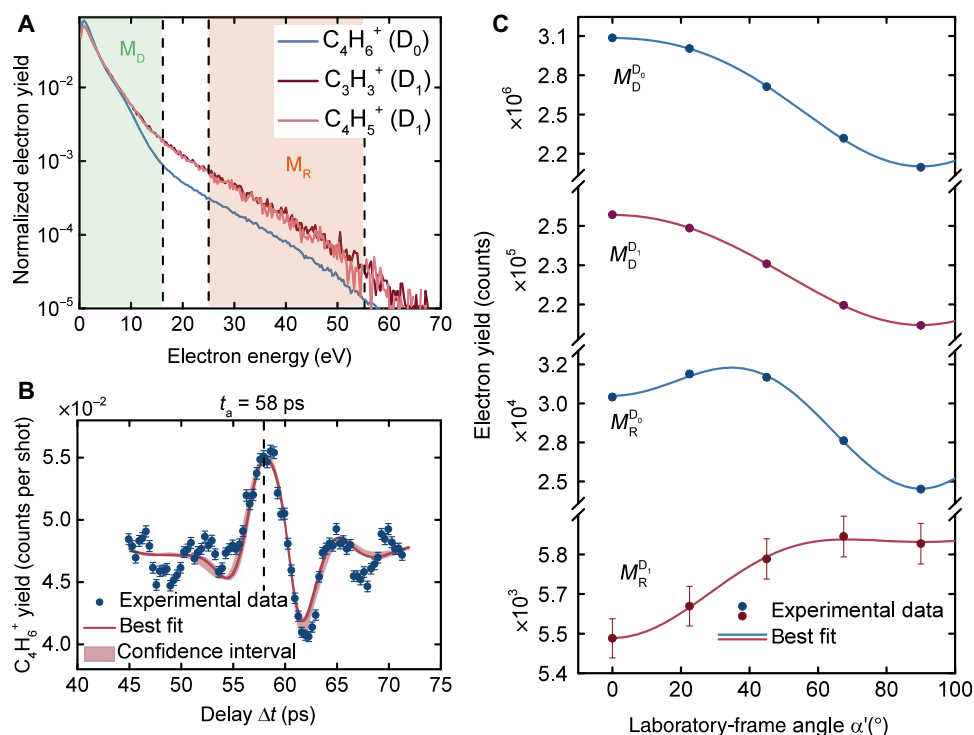
Fig. 2. Experimental data. (**A**) Electron kinetic energy distributions acquired in coincidence with different ion species, allowing one to distinguish between the D_0 and D_1 ionization channels. The distributions are normalized to the same total yield for better comparison. The green and orange areas indicate integration limits for the determination of the yields of direct (M_D) and rescattered (M_R) electrons, respectively, in the angle-dependent data in (C). (**B**) Delay scan of the nonadiabatic alignment, showing the 1,3-butadiene parent ion yield around the rotational half-revival. The error bars are given by counting statistics. Shown as a red solid line and shaded area are the best fits and confidence intervals from the extraction procedure of the alignment distribution, which uses a symmetric-top approximation. The experimental data shown in (C) were acquired at the delay t_a corresponding to peak alignment. (**C**) Channel-resolved yield of direct ($M_D^{D_0}, M_D^{D_1}$) and rescattered ($M_R^{D_0}, M_R^{D_1}$) electrons as a function of the angle α' between the polarizations of the alignment and SFI laser fields, using the integration limits shown in (A). Solid lines denote best fits from the deconvolution of the molecular-frame ionization and rescattering probabilities using the known alignment distribution. Error bars, given by counting statistics, are smaller than the symbols used for $M_D^{D_0}$, $M_D^{D_1}$, and $M_R^{D_0}$.

attributed to the different SFI wavelengths used [$\lambda = 1290$ nm versus $\lambda = 800$ nm in the work of Mikosch et al. (24)]. Use of this $S(\theta)$ permits the determination of the $R(\theta) \times Q(\theta)$ distributions from $M_R(\alpha')$. These distributions are plotted in Fig. 3C for the two SFI channels. The solid lines represent the most likely distribution resulting from the experiment, whereas the shaded areas reflect the confidence intervals that arise from the alignment deconvolution and from the propagation of the statistical errors (see the Supplementary Materials).

Figure 3C shows unambiguously that the experimental channel-specific product of the return probability $R(\theta)$ and the high-angle scattering probability $Q(\theta)$ differs significantly between D_0 and D_1, both in shape and in amplitude. Note that the probability $R(\theta) \times Q(\theta)$ is plotted on an absolute scale. Depending on the molecular-frame polar angle along which the laser is polarized, between 0.75 and 1.30% of the continuum electrons rescatter in the D_0 SFI channel. The rescattering probability is significantly higher in the D_1 SFI channel, namely, between 1.85 and 3.05%. In both channels, $R(\theta) \times Q(\theta)$ displays a pronounced minimum for polarization of the strong laser field along the long axis of the molecule ($\theta = 0°$). In this direction, the respective ionization probabilities (see Fig. 3A) are both maximal. However, for the D_0 SFI channel, the rescattering probability distribution peaks at $\theta \approx 60°/120°$, whereas for the D_1 channel, we find $R(\theta) \times Q(\theta)$ to be maximal for orthogonal polarization ($\theta = 90°$), where the D_0 channel displays a shallow minimum.

To independently corroborate our experimental results, we performed numerical calculations using the time-dependent resolution-in-ionic-states (TD-RIS) theory method (29). Perfectly one-dimensionally aligned molecules were used in the model while averaging over the azimuthal angle ϕ. Because of the very substantial computational cost, the simulations had to be conducted for dedicated half-cycle (ionization) and few-cycle (recollision) laser pulses at $\lambda = 800$ nm (see the Supplementary Materials). The derived angle- and channel-resolved ionization [$S(\theta)$] and the derived rescattering [$R(\theta) \times Q(\theta)$] probabilities are plotted in Fig. 3 (B and D, respectively) and can be compared with their experimental counterparts in Fig. 3, A and C. There is good qualitative agreement between the experimentally and computationally obtained ionization probabilities $S(\theta)$ for both SFI channels, in accordance with the earlier SFI study at $\lambda = 800$ nm (24). The calculations confirm the observation from experiment that the $R(\theta) \times Q(\theta)$ distributions for D_0 and D_1 display clear differences. Although the calculated distributions, plotted in Fig. 3D, are outside the confidence intervals of the experiment plotted in Fig. 3C, there is good qualitative agreement, especially keeping in mind the limitations of the theoretical model in considering the laser pulse (see the Supplementary Materials). The theory results for $R(\theta) \times Q(\theta)$ reproduce all key features found in the experiment: the pronounced minimum in the distribution for $\theta = 0°$ in both the D_0 and the D_1 channel, the maxima at $\theta \approx 60°/120°$ in the D_0 channel and at $\theta = 90°$ in the D_1 channel, and the dip at $\theta = 90°$ in the D_0 channel.
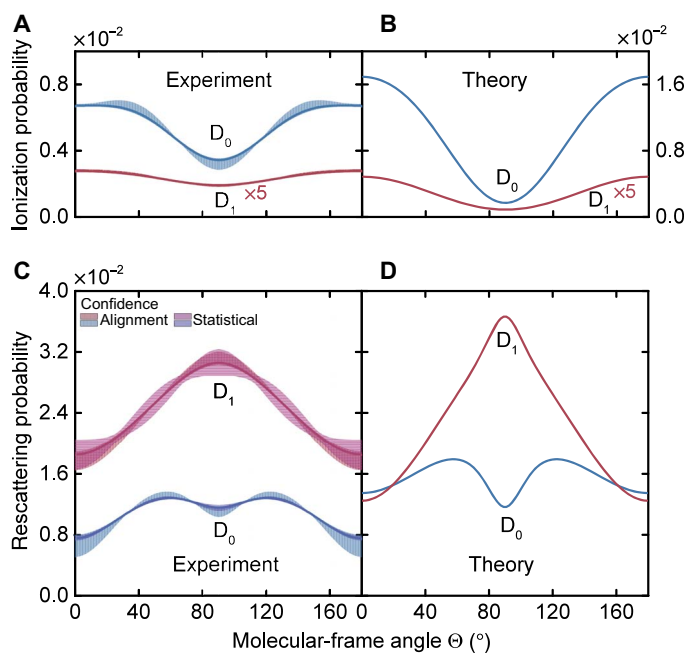
Fig. 3. Effect of the shape of the continuum wave packet on rescattering. (**A** and **C**) Channel-resolved molecular-frame polar angle–dependent ionization probability $S(\theta)$ (A) and rescattering probability $R(\theta) \times Q(\theta)$ (C), as obtained from the deconvolution of the experimental data shown in Fig. 2C with the alignment distribution of the molecular ensemble. The shaded areas delimit the confidence intervals arising from the uncertainty of the alignment distribution (vertical shading) and from the statistical error of the measurements in Fig. 2C (horizontal shading) (see the Supplementary Materials). The latter error contributes significantly only to the D_1 rescattering probability. (**B** and **D**) The same observables as in (A) and (C) obtained from the TD-RIS calculation. Note that while the ionization probability of the D_0 channel in (A) and (B) has been scaled arbitrarily, the relative scale between D_0 and D_1 reflects their contributions to ionization.

To assist in the interpretation of our results, we performed another TD-RIS calculation: We simulated laser-induced electron scattering where, at the outer turning point of the laser-driven continuum electron motion, the actual channel-dependent continuum wave packet was substituted by the same artificial Gaussian continuum wave packet for both SFI channels. This Gaussian wave packet is then driven back toward the cation where scattering occurs. Figure 4A shows an iso-surface of the Gaussian electron wave packet as created at the outer turning point and shortly after the electron-ion scattering event, for a molecule aligned perpendicular to the laser polarization axis. The phase of the wave packet is depicted as a color scale, so that a color gradient indicates a moving wave packet. The transverse and longitudinal width of the initial Gaussian wave packet was set to 6.3 a_0, similar to the spatial separation of the outermost carbon atoms in the 1,3-butadiene molecule. This choice ensures that (i) most of the wave packet recollides and that (ii) upon recollision, the wavefront is, to a good approximation, planar, as can be seen from the parallel stripes indicating the phase gradient. Our model is, hence, reminiscent of the conventional diffraction of electron beams (30) but ensures that, under the influence of the laser field, the colliding electrons feature a kinetic energy distribution very similar to the one in the recollision experiment presented below. Because the return probability R is independent of θ by design in this simulation, we can determine the high-angle scattering probability $Q(\theta)$ as a function of the molecular-frame polar angle θ
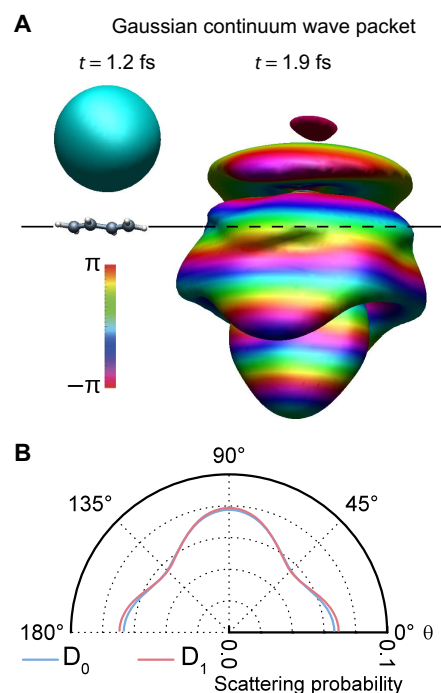
Fig. 4. Channel indepedence of the high-angle scattering probability. Simulated strong laser field–driven scattering of a three-dimensional Gaussian continuum wave packet (replacing the actual channel-dependent wave packet launched by SFI) off the $C_4H_6^+$ 1,3-butadiene ion in the electronic ground state (D_0) and in the first excited state (D_1). (**A**) Snapshots of the electron density isosurfaces (of value $2.5 \times 10^{-5} a_0^{-3}$, where a_0 is the Bohr radius) at two instants in time during the 2.7-fs period laser field (see the Supplementary Materials), for a laser polarization perpendicular to the plane of the molecule ($\theta = 90°$, $\phi = 90°$) and the ion in the D_0 ground state. For the definition of θ and ϕ, see the coordinate system in Fig. 1. The maximum of the oscillatory electric field defines zero time. The color scale describing the phase of the electron wave function is the same as in Fig. 1. (**B**) Comparison of the computationally obtained θ-dependent, ϕ-averaged scattering probability $R(\theta) \times Q(\theta)$ for a Gaussian wave packet scattering off the $C_4H_6^+$ ion in the D_0 and the D_1 state. Because the return probability $R(\theta)$ is channel- and angle-independent by design in this calculation [that is, $R(\theta) = R$], the calculation proves that the high-angle scattering probability $Q(\theta)$ is near-independent of the electronic state of the 1,3-butadiene molecular cation, as expected.

of the laser polarization, averaging over the azimuthal molecular-frame angle ϕ. $Q(\theta)$ is plotted in Fig. 4B for the D_0 (blue) and the D_1 (red) cation (see the Supplementary Materials for further details). Although a characteristic distribution is observed, almost no difference is found between the two ionic states. This observation confirms our expectation that $Q(\theta)$ does not depend on the state of the 1,3-butadiene cations (see Introduction).

DISCUSSION
Given the identical high-angle scattering probability distributions $Q(\theta)$ for both channels, the channel dependence of the molecular-frame rescattering probability $R(\theta) \times Q(\theta)$, observed both experimentally and in the TD-RIS calculations, is a remarkable result. Note that the computed $Q(\theta)$ in Fig. 4B features a rather different angular dependence compared to both of the channel-dependent $R(\theta) \times Q(\theta)$ distributions. These findings imply that the molecular-frame return probability distribution $R(\theta)$ depends both on the ionization channel and on the

angle of the laser polarization with respect to the molecular frame. In other words, contrary to the expectations of the simple SFA theories, $R(\theta)$ is a distribution that is strongly system-dependent.

The molecular-frame and channel dependence of $R(\theta)$ is understood in terms of the Dyson orbitals associated with the two continuum channels (Fig. 1, A and B). The nodal planes of the Dyson orbitals are much more strongly reflected in the channel-specific rescattering probability distributions (Fig. 3, C and D) than in the ionization probability distributions (Fig. 3, A and B). We argue that this is the result of the continuum propagation, during which the structure of the respective Dyson orbital is preserved and expanded. To strong-field ionize a molecule with a field directed along the nodal plane of a Dyson orbital, the outgoing photoelectron must acquire nonzero transverse momentum (16, 31). The momentum increases when the spacing between the lobes separated by the nodal plane decreases. The transverse spread of the wave packet strongly decreases the probability of recollision, particularly that of recollision leading to high-angle scattering, for which small impact parameters are required.

In 1,3-butadiene, the pronounced minimum of the rescattering probability found for both D_0 and D_1 for molecular alignment along the laser polarization axis ($\theta = 0°$) (see Fig. 3, C and D) coincides with a node in the plane of the molecule for both Dyson orbitals. In contrast, the molecular-frame ionization probabilities feature maxima for a laser field pointing in this direction (see Fig. 3, A and B). For parallel alignment, the continuum wave packets are expected to appear as narrow bimodal distributions for both D_0 and D_1, due to the structure of the Dyson orbitals. Because of their high transverse velocity, these wave packets will largely miss the molecule after propagation. For perpendicular polarization of the strong laser field ($\theta = 90°$), on the other hand, the two SFI channels feature a rather different Dyson orbital structure. There is a nodal plane for the D_0 Dyson orbital for all azimuthal angles ϕ (see Fig. 1A). During laser-driven propagation, the two lobes associated with maximal electron density (shown in Fig. 1A for a laser polarization perpendicular to the plane of the molecule) broaden and evolve away from the molecule. Hence, we expect a local minimum in the rescattering probability, in agreement with the observation (see Fig. 3, C and D). Because the separation between the lobes in the D_0 Dyson orbital is larger for $\theta = 90°$ than for $\theta = 0°$, the transverse velocity of the continuum wave packet is smaller for perpendicular than for parallel polarization. Consequently, a somewhat higher fraction of the wave packet returns to the core for perpendicular polarization, and the minimum in the rescattering probability at $\theta = 90°$ is less pronounced than the minimum at $\theta = 0°$, in line with the experimental finding. In contrast, for the D_1 Dyson orbital, maxima are found in the ϕ-dependent wave function amplitude when the laser is polarized perpendicular to the plane of the molecule, and nodes are found when the laser is polarized in the plane of the molecule (see Fig. 1B). The ϕ-averaged, θ-dependent integrated amplitude therefore features a maximum for perpendicular polarization, and the recollision probability peaks for $\theta = 90°$ (see Fig. 3, C and D). We note that different continuum propagation time intervals are encoded in the electron momentum maps originating from rescattering (32), which will be exploited in future work.

While 1,3-butadiene allows us to separate different SFI channels in a convenient fashion, we believe that there is nothing special about the molecule used regarding its recollision dynamics. 1,3-Butadiene can be regarded as a model system representative for molecules featuring nodal planes. We hence anticipate that our findings of molecular orbital imprint in laser-driven electron recollision are of general nature. Our

results caution that the relative contribution of different SFI channels to HHG and LIED probes of molecular dynamics (25, 33–35) is not simply reflected by the SFI yield and by the interaction cross sections associated with these channels. Moreover, our findings are highly relevant for the interpretation of both LIED and HHG experiments within the SFA, including the quantitative rescattering theory (36). For instance, in LIED, the momentum distribution of electrons undergoing a single rescattering event along the long trajectory is given in the molecular frame by $D(\vec{p}, \theta) = W(p_r, \theta)\sigma(p_r, \vartheta_r, \theta)$. Here, p_r denotes the momentum upon return, ϑ_r indicates the scattering angle, W denotes the amplitude of the returning wave packet, and σ indicates the desired DCS containing the structural information of the molecule (11). The final momentum of the electron $\vec{p}$ differs from the electron momentum after scattering (defined by p_r and ϑ_r) by the vector potential at the instant of recollision. Thus far, a separation ansatz $W(p_r, \theta) = S(\theta) \times W'(p_r)$ is usually made when analyzing LIED photoelectron momentum distributions measured for unaligned and aligned molecular samples (11, 13, 15). This ansatz separates the amplitude of the returning wave packet into the angular-dependent ionization probability $S(\theta)$ and an angle-independent return probability $W'(p_r)$ that depends exclusively on the return momentum. $S(\theta)$ is determined by a calculation (11, 13). Our findings show that the return probability is both molecular frame– and SFI channel–dependent. An approximation that is presently made in the interpretation of LIED and HHG experiments is not universally valid and has to be complemented by an experimental or theoretical analysis of the continuum propagation as presented here. Note that, from the perspective of formal theory (see section S7), the factorization ansatz $S(\theta) \times R(\theta) \times Q(\theta)$ itself can come under scrutiny near nodal planes owing to the wave packet coherence preserved in the propagation and interaction.

The fact that the return probability is molecular frame– and SFI channel–dependent, as established here, is inherent to continuum propagation and hence expected to be universal. We anticipate that the observed effect increases in importance for mid-infrared laser fields (37), where subcycle excursion times are longer than those for laser fields in the near-infrared, allowing more time for continuum evolution.

MATERIALS AND METHODS
Experimental details
In the experiment, we used a home-built reaction microscope (REMI) (26) to measure the photoelectron momentum from the SFI of 1,3-butadiene molecules in coincidence with the ion mass. The applied electric and magnetic field strengths were $E = 30$ V/cm and $B = 17$ G, respectively. We limited the detected ionization rate to ≤0.2 events per shot to minimize the occurrence of false coincidences. In addition, we implemented further measures to filter out uncorrelated events in the acquired data (see the Supplementary Materials). In this way, we ensured that the overwhelming majority of electrons and ions detected in coincidence originated from the same ionization event. Linearly polarized laser pulses with a central wavelength of $\lambda = 1290$ nm, a pulse duration of 40 fs, an energy per pulse of 23 μJ, and a repetition rate of 10 kHz were used. These were derived by frequency conversion of pulses from an amplified Ti:Sa laser system (Amplitude Technologies) in a commercial optical parametric amplifier (TOPAS, Light Conversion). For one-dimensional field-free spatial alignment of the supersonically cooled molecules, a nonadiabatic scheme was used (38). Fundamental pulses of the 800-nm wavelength Ti:Sa laser system were temporally stretched to a pulse duration of 0.55 ps and applied 58 ps

before the 1290-nm pulses, such that the recollision experiment took place at the rotational half-revival. No ionization yield resulted from the alignment pulses alone. A motorized waveplate in the alignment laser arm was used to vary α', the laboratory-frame angle between the linear polarizations of the alignment and SFI pulses. To obtain enough statistics in the weak rescattering tail for both SFI channels, data were acquired at just five different α' angles. The data were accumulated in random order over many short measuring intervals for the different angles to minimize the effects of potential small variations of the laser parameters. In total, each photoelectron spectrum contains the events of 3.8×10^8 laser shots (10.5 hours of data acquisition at the 10-kHz repetition rate of the laser). Further experimental details can be found in the Supplementary Materials.

Deconvolution of molecular-frame properties from laboratory-frame observables

Laboratory-frame experimental observables measured for aligned molecules derived from a convolution of the molecular-frame molecular properties with the probability distribution of molecular axis alignment angles. We used primed (unprimed) characters for laboratory-frame (molecular-frame) parameters. Assuming azimuthal symmetry, the equation

$$M_X(\alpha') = 1/(8\pi^2) \times \int_0^{2\pi} d\phi' \int_0^{\pi} d\theta' X[\theta(\theta', \phi'; \alpha')] \times A(\theta')\sin\theta' \quad (1)$$

$$\cos\theta = \cos\alpha'\cos\theta' - \sin\alpha'\sin\theta'\sin\phi' \quad (2)$$

was used to deconvolve the molecular-frame property $X(\theta)$ by fitting the experimental observable $M_X(\alpha')$, using the most probable alignment distribution $A(\theta')$ (see section S6). θ' and ϕ' are the polar and azimuthal laboratory-frame angles, respectively; θ is the polar molecular-frame angle; and α' is the relative laboratory-frame angle between the polarizations of the alignment and the SFI laser pulses. $X(\theta)$ was parameterized by a sum of even Legendre polynomials (even, because we used aligned, not oriented molecules) according to

$$X(\theta) = \sum_{k=0}^{k_{max}} b_{2k} P_{2k}(\cos\theta) \quad (3)$$

where the b_{2k} are fit parameters. For the laboratory-frame observables in this study (see Fig. 2C), the polynomial was terminated at $k_{max} = 2$ to not overparameterize the fits to the limited number of experimental data points. For the determination of the confidence intervals shown in Fig. 2, see the Supplementary Materials.

Coupled channels rescattering simulations

The strong field–driven recollision dynamics were simulated using the TD-RIS method (29). Here, we present the first application of TD-RIS to the simulation of three-dimensional photoelectron spectra including recollision.

TD-RIS combines ab initio quantum chemistry for the computation of multielectron wave functions with single-particle time-dependent numerical grid solutions. The field-free n-electron neutral state ($|N\rangle$) and the lowest few ($n-1$)-electron singly ionized states ($|I_m\rangle$) were used as the basis. The wave function of the nth continuum electron associated with each ionic state was represented on a three-dimensional Cartesian

numerical grid. The coupling to the laser field was treated in the dipole approximation and length gauge.

In TD-RIS, the ansatz for the n-electron wave function is

$$|\Psi(t)\rangle = b(t)|\tilde{N}\rangle + \sum_m \left[a_m(t)|\tilde{\phi}_m^S\rangle|I_m\rangle + |\chi_m(t)\rangle|I_m\rangle \right] \quad (4)$$

where $|\chi_m(t)\rangle$ is the one-electron continuum wave packet associated with ionic state m and $|\tilde{\phi}_m^S\rangle$ is the normalized source orbital, which is related to the Dyson orbital $|\psi_m^D\rangle$ by

$$|\tilde{\phi}_m^S\rangle = \frac{|\psi_m^D\rangle}{\sqrt{\langle\psi_m^D\psi_m^D\rangle}}$$

with $|\psi_m^D\rangle = \sqrt{n}\langle I_m|N\rangle$. Finally, $|\tilde{N}\rangle$ is the normalized component of the neutral ground state $|N\rangle$ orthogonal to the set of source ion states $|\tilde{\phi}_m^S\rangle|I_m\rangle$. Inserting the ansatz (Eq. 4) into the time-dependent Schrödinger equation leads to (after some manipulations) coupled equations for the amplitudes $b(t)$, $a_m(t)$, and the respective one-electron continuum wave packets $|\chi_m(t)\rangle$, which were represented on three-dimensional Cartesian grids. For further details, see the study of Spanner and Patchkovskii (29). The coupled equations are solved numerically using the leap-frog algorithm. For computational details, the reader is referred to the Supplementary Materials.

REFERENCES AND NOTES

1. K. J. Schafer, B. Yang, L. F. DiMauro, K. C. Kulander, Above threshold ionization beyond the high harmonic cutoff. *Phys. Rev. Lett.* **70**, 1599–1602 (1993).
2. P. B. Corkum, Plasma perspective on strong field multiphoton ionization. *Phys. Rev. Lett.* **71**, 1994–1997 (1993).
3. A. L'Huillier, L. A. Lompre, G. Mainfray, C. Manus, Multiply charged ions formed by multiphoton absorption processes in the continuum. *Phys. Rev. Lett.* **48**, 1814–1817 (1982).
4. B. Walker, B. Sheehy, L. F. DiMauro, P. Agostini, K. J. Schafer, K. C. Kulander, Precision measurement of strong field double ionization of helium. *Phys. Rev. Lett.* **73**, 1227–1230 (1994).

5. V. R. Bhardwaj, D. M. Rayner, D. M. Villenueve, P. B. Corkum, Quantum interference in double ionization and fragmentation of C_6H_6 in intense laser fields. *Phys. Rev. Lett.* **87**, 253003 (2001).

6. M. Oppermann, S. J. Weber, L. J. Frasinski, M. Yu. Ivanov, J. P. Marangos, Multichannel contributions in the nonsequential double ionization of CO_2. *Phys. Rev. A* **88**, 043432 (2013).

7. T. Zuo, A. D. Bandrauk, P. B. Corkum, Laser-induced electron diffraction: A new tool for probing ultrafast molecular dynamics. *Chem. Phys. Lett.* **259**, 313–320 (1996).

8. M. Lein, J. P. Marangos, P. L. Knight, Electron diffraction in above-threshold ionization of molecules. *Phys. Rev. A* **66**, 051404 (2002).

9. M. Spanner, O. Smirnova, P. B. Corkum, M. Y. Ivanov, Reading diffraction images in strong field ionization of diatomic molecules. *J. Phys. B At. Mol. Opt. Phys.* **37**, L243 (2004).

10. M. Meckel, D. Comtois, D. Zeidler, A. Staudte, D. Pavičić, H. C. Bandulet, H. Pépin, J. C. Kieffer, R. Dörner, D. M. Villeneuve, P. B. Corkum, Laser-induced electron tunneling and diffraction. *Science* **320**, 1478–1482 (2008).

11. C. I. Blaga, J. Xu, A. D. DiChiara, E. Sistrunk, K. Zhang, P. Agostini, T. A. Miller, L. F. DiMauro, C. D. Lin, Imaging ultrafast molecular dynamics with laser-induced electron diffraction. *Nature* **483**, 194–197 (2012).

12. J. Xu, C. I. Blaga, K. Zhang, Y. H. Lai, C. D. Lin, T. A. Miller, P. Agostini, L. F. DiMauro, Diffraction using laser-driven broadband electron wave packets. *Nat. Commun.* **5**, 4635 (2014).

13. M. G. Pullen, B. Wolter, A.-T. Le, M. Baudisch, M. Hemmer, A. Senftleben, C. D. Schröter, J. Ullrich, R. Moshammer, C. D. Lin, J. Biegert, Imaging an aligned polyatomic molecule with laser-induced electron diffraction. *Nat. Commun.* **6**, 7262 (2015).

14. M. G. Pullen, B. Wolter, A.-T. Le, M. Baudisch, M. Sclafani, H. Pires, C. D. Schröter, J. Ullrich, R. Moshammer, T. Pfeifer, C. D. Lin, J. Biegert, Influence of orbital symmetry on diffraction imaging with rescattering electron wave packets. *Nat. Commun.* **7**, 11922 (2016).

15. Y. Ito, C. Wang, A.-T. Le, M. Okunishi, D. Ding, C. D. Lin, K. Ueda, Extracting conformational structure information of benzene molecules via laser-induced electron diffraction. *Struct. Dyn.* **3**, 034303 (2016).

16. M. Lein, Antibonding molecular orbitals under the influence of elliptically polarized intense light. *J. Phys. B At. Mol. Opt. Phys.* **36**, L155 (2003).

17. M. Meckel, A. Staudte, S. Patchkovskii, D. M. Villeneuve, P. B. Corkum, R. Dörner, M. Spanner, Signatures of the continuum electron phase in molecular strong-field photoelectron holography. *Nat. Phys.* **10**, 594–600 (2014).

18. O. Smirnova, M. Ivanov, Multielectron high harmonic generation: Simple man on a complex plane, in *Attosecond and XUV Spectroscopy: Ultrafast Dynamics and Spectroscopy*, T. Schultz, M. Vrakking, Eds. (Wiley, 2014), pp. 201–256.

19. A.-T. Le, H. Wei, C. Jin, C. D. Lin, Strong-field approximation and its extension for high-order harmonic generation with mid-infrared lasers. *J. Phys. B At. Mol. Opt. Phys.* **49**, 053001 (2016).

20. T. Morishita, O. I. Tolstikhin, Adiabatic theory of strong-field photoelectron momentum distributions near a backward rescattering caustic. *Phys. Rev. A* **96**, 053416 (2017).

21. O. Smirnova, Y. Mairesse, S. Patchkovskii, N. Dudovich, D. Villeneuve, P. Corkum, M. Yu. Ivanov, High harmonic interferometry of multi-electron dynamics in molecules. *Nature* **460**, 972–977 (2009).

22. A. E. Boguslavskiy, J. Mikosch, A. Gijsbertsen, M. Spanner, S. Patchkovskii, N. Gador, M. J. J. Vrakking, A. Stolow, The multielectron ionization dynamics underlying attosecond strong-field spectroscopies. *Science* **335**, 1336–1340 (2012).

23. D. Pavičić, K. F. Lee, D. M. Rayner, P. B. Corkum, D. M. Villeneuve, Direct measurement of the angular dependence of ionization for N_2, O_2, and CO_2 in intense laser fields. *Phys. Rev. Lett.* **98**, 243001 (2007).

24. J. Mikosch, A. E. Boguslavskiy, I. Wilkinson, M. Spanner, S. Patchkovskii, A. Stolow, Channel- and angle-resolved above threshold ionization in the molecular frame. *Phys. Rev. Lett.* **110**, 023004 (2013).

25. B. Wolter, M. G. Pullen, A.-T. Le, M. Baudisch, K. Doblhoff-Dier, A. Senftleben, M. Hemmer, C. D. Schröter, J. Ullrich, T. Pfeifer, R. Moshammer, S. Gräfe, O. Vendrell, C. D. Lin, J. Biegert, Ultrafast electron diffraction imaging of bond breaking in di-ionized acetylene. *Science* **354**, 308–312 (2016).

26. J. Ullrich, R. Moshammer, A. Dorn, R. Dörner, L. Ph. H. Schmidt, H. Schmidt-Böcking, Recoil-ion and electron momentum spectroscopy: Reaction-microscopes. *Rep. Prog. Phys.* **66**, 1463 (2003).

27. F. Rosca-Pruna, M. J. J. Vrakking, Experimental observation of revival structures in picosecond laser-induced alignment of I_2. *Phys. Rev. Lett.* **87**, 153902 (2001).

28. J. Mikosch, C. Z. Bisgaard, A. E. Boguslavskiy, I. Wilkinson, A. Stolow, The quantitative determination of laser-induced molecular axis alignment. *J. Chem. Phys.* **139**, 024304 (2013).

29. M. Spanner, S. Patchkovskii, One-electron ionization of multielectron systems in strong nonresonant laser fields. *Phys. Rev. A* **80**, 063411 (2009).

30. I. Hargittai, M. Hargittai, *Stereochemical Applications of Gas-Phase Electron Diffraction* (VCH, 1998).

31. R. Murray, W.-K. Liu, M. Yu. Ivanov, Partial fourier-transform approach to tunnel ionization: Atomic systems. *Phys. Rev. A* **81**, 023413 (2010).

32. Z. Chang, *Fundamentals of Attosecond Optics* (CRC Press, 2011).

33. W. Li, X. Zhou, R. Lock, S. Patchkovskii, A. Stolow, H. C. Kapteyn, M. M. Murnane, Time-resolved dynamics in N_2O_4 probed using high harmonic generation. *Science* **322**, 1207–1211 (2008).

34. H. J. Wörner, J. B. Bertrand, B. Fabre, J. Higuet, H. Ruf, A. Dubrouil, S. Patchkovskii, M. Spanner, Y. Mairesse, V. Blanchet, E. Mével, E. Constant, P. B. Corkum, D. M. Villeneuve, Conical intersection dynamics in NO_2 probed by homodyne high-harmonic spectroscopy. *Science* **334**, 208–212 (2011).

35. S. G. Walt, N. Bhargava Ram, M. Atala, N. I. Shvetsov-Shilovski, A. von Conta, D. Baykusheva, M. Lein, H. J. Wörner, Dynamics of valence-shell electrons and nuclei probed by strong-field holography and rescattering. *Nat. Commun.* **8**, 15651 (2017).

36. Z. Chen, A.-T. Le, T. Morishita, C. D. Lin, Quantitative rescattering theory for laser-induced high-energy plateau photoelectron spectra. *Phys. Rev. A* **79**, 033409 (2009).

37. B. Wolter, M. G. Pullen, M. Baudisch, M. Sclafani, M. Hemmer, A. Senftleben, C. D. Schröter, J. Ullrich, R. Moshammer, J. Biegert, Strong-field physics with Mid-IR fields. *Phys. Rev. X* **5**, 021034 (2015).

38. H. Stapelfeldt, T. Seideman, *Colloquium*: Aligning molecules with strong laser pulses. *Rev. Mod. Phys.* **75**, 543–557 (2003).

39. M. W. Schmidt, K. K. Baldridge, J. A. Boatz, S. T. Elbert, M. S. Gordon, J. H. Jensen, S. Koseki, N. Matsunaga, K. A. Nguyen, S. Su, T. L. Windus, M. Dupuis, J. A. Montgomery Jr., General atomic and molecular electronic structure system. *J. Comput. Chem.* **14**, 1347–1363 (1993).

40. M. E. Jacox, Vibrational and electronic energy levels of polyatomic transient molecules. Supplement A. *J. Phys. Chem. Ref. Data* **27**, 115–393 (1998).

41. S. Patchkovskii, Z. Zhao, T. Brabec, D. M. Villeneuve, High harmonic generation and molecular orbital tomography in multielectron systems. *J. Chem. Phys.* **126**, 114306 (2007).

42. C. Z. Bisgaard, "Laser induced alignment," thesis, University of Aarhus (2006).